Progress in Physics of Applied Materials 6 (2026), Serial Number 11, 151–162

Semnan University

Progress in Physics of Applied Materials

journal homepage: https://ppam.semnan.ac.ir/

$BaFe_{12}O_{19}$/rGO Nanocomposites: A Comprehensive Study of Structural, Optical, and Magnetic Properties

Mehrabani, Mona[a*], Ghazi, Mohammad Ebrahim, Izadifard, Morteza

Faculty of Physics, Shahrood University of Technology, Shahrood, Iran

ARTICLE INFO

Article history:
Received: 6 October 2025
Revised: 19 November 2025
Accepted: 28 November 2025
Published online: 17 December 2025

Keywords:
Hexaferrite;
$BaFe_{12}O_{19}$/rGO nanocomposites;
Optical properties;
Magnetic properties.

ABSTRACT

This work investigates the synthesis and properties of barium hexaferrite ($BaFe_{12}O_{19}$) and its Reduced Graphene Oxide (rGO) nanocomposites using the auto-combustion sol-gel method. $BaFe_{12}O_{19}$ is known to have certain limitations in practical applications, which motivates the development of $BaFe_{12}O_{19}$-based nanocomposites with carbon-based materials such as rGO to enhance their multifunctional behavior. The study explores the impact of different rGO content (10%, 20%, 40%, and 50% Wt.%) on the nanocomposites' structural, optical, and magnetic properties. The techniques, including X-ray diffraction (XRD), field emission scanning electron microscopy (FESEM), and magnetic hysteresis measurements were used to characterize the samples. The structural studies revealed the formation of nanocomposite. Optical studies indicated that the band gap energy decreased from 1.62 eV for pure $BaFe_{12}O_{19}$ to 1.48 eV for the composite containing 50% rGO. Concurrently, magnetic hysteresis measurements showed a reduction in saturation magnetization, from 54.21 emu/g for pure $BaFe_{12}O_{19}$ to 23.38 emu/g for the 50% rGO composite.

1. Introduction

Barium hexaferrite ($BaFe_{12}O_{19}$), also known as M-type hexaferrite, has attracted considerable attention in the fields of materials science and engineering due to its unique magnetic and physical properties [1]. This ceramic material, characterized by its hexagonal crystal structure, exhibits high saturation magnetization [2], significant coercivity [3], chemical stability [4], and high thermal resistance [5], making it suitable for a wide range of industrial applications [6]. These applications include the manufacture of electromagnetic devices, magnetic storage media, electric motors, microwave devices, and advanced sensors [7]. The versatility of barium hexaferrite in these fields is attributed to its remarkable combination of magnetic, electrical, and mechanical properties [8]. Over the years, various methods have been developed for the synthesis of barium hexaferrite, such as sol-gel processes [9], hydrothermal techniques [10], chemical deposition [11], and solid-state reactions [12]. Achieving the desired material properties requires careful control of parameters such as temperature, pressure, and chemical composition. Among these techniques, the auto-combustion method stands out for its simplicity, efficiency, and ability to produce high-purity, crystalline materials. This process relies on a self-sustaining oxidation-reduction reaction, providing the necessary energy for the synthesis process and resulting in a product with excellent chemical uniformity [13]. While barium hexaferrite possesses many desirable properties, challenges such as high electrical resistivity can limit its performance in certain applications. To overcome these limitations, researchers have turned to composite materials, combining barium hexaferrite with nanomaterials, especially two-dimensional materials like graphene [14]. Graphene, a monolayer of carbon atoms arranged in a two-dimensional hexagonal lattice, is distinguished by its

* Corresponding author.
E-mail address: mona.mehrabanii@gmail.com

Cite this article as:
Mehrabani, M., Ghazi, M.E. and Izadifard, M., 2026. BaFe12O19/rGO Nanocomposites: A Comprehensive Study of Structural, Optical, and Magnetic Properties. *Progress in Physics of Applied Materials*, *6*(2), pp.151-162. DOI: 10.22075/ppam.2025.39111.1172

exceptional electrical conductivity, outstanding mechanical resilience, extensive surface area, and remarkable thermal and electromagnetic wave absorption properties [15, 16]. The integration of graphene into barium hexaferrite enhances the composite's overall performance by reducing electrical resistivity, improving microwave absorption capabilities, and increasing the mechanical strength and thermal stability of the material [17]. Graphene also plays a crucial role in facilitating the uniform dispersion of barium hexaferrite nanoparticles, which improves the magnetic properties and structural integrity of the composite. These enhanced composites show promise for applications in electromagnetic interference shielding, microwave devices, and sensors, as well as in energy storage systems and high-temperature industrial environments [18,19]. This composite material paves the way for the advancement of multifunctional materials with integrated properties, tailored to meet diverse requirements in fields such as electronics, biomedicine, energy storage, and beyond. Nevertheless, achieving optimal performance and targeted applications depends heavily on the specific demands of each use case. Within academic research, numerous studies have highlighted the relationship between material characteristics and processing techniques. Jie *et al.* utilized a composite of $BaFe_{12}O_{19}$/graphene/polyaniline applied through a coating method on flexible fabrics, aiming to enhance microwave absorption, with a particular emphasis on the crucial role of graphene in improving electrical conductivity, thermal stability, and overall absorption efficiency [20]. Wang *et al.* developed a flexible and robust multilayer composite fabric coated with $BaFe_{12}O_{19}$ / graphene oxide (GO), aiming to achieve high-performance electromagnetic shielding and microwave absorption, highlighting the synergy between $BaFe_{12}O_{19}$ and GO for enhanced absorption efficiency, mechanical strength, and durability [21]. Moreover, Mehrabani *et al.* investigated the influence of GO content on the optical, magnetic, and dielectric properties of $BaFe_{12}O_{19}$/GO nanocomposites, demonstrating that variations in graphene oxide concentration significantly affect the structural, magnetic, and electromagnetic behavior of the resulting materials [22].

This study examined the influence of rGO content on the properties of the composites, offering insights for optimizing their performance in applications including electronics, energy storage, and electromagnetic devices. The research enhances our understanding of $BaFe_{12}O_{19}$/rGO composites while emphasizing the importance of rGO concentration in adjusting the material's functionality. By varying the rGO weight percentages (10%, 20%, 40%, and 50%) and analyzing their magnetic characteristics, we can identify the most suitable configurations for applications in magnetic recording and memory devices, which will be discussed in greater detail in the following sections.

2. Experimental procedures and details

2.1. Synthesis of $BaFe_{12}O_{19}$

The Auto-Combustion Route (ACR) sol–gel method was employed as a cost-effective and efficient approach for synthesizing nanoparticles [23]. The materials used for the synthesis included Iron (III) Nitrate Hexahydrate ($Fe(NO_3)_3{\cdot}9H_2O$, Merck 99%), Barium Nitrate ($Ba(NO_3)_2$, Merck 99%), and Ammonia (25% NH_3), all of which were analytical grade and sourced from Merck. $Fe(NO_3)_3{\cdot}9H_2O$ and $Ba(NO_3)_2$ were selected as starting materials, while citric acid (Merck 99%) was employed as a fuel. The synthesis process was carried out with a molar ratio of Ba:Fe set at 1:11 and a metal-to-fuel ratio of 1:13. It is worth noting that the nominal stoichiometric ratio of Ba:Fe in $BaFe_{12}O_{19}$ is 1:12; however, in this study, a slightly reduced Ba:Fe molar ratio of 1:11 was intentionally employed. This deviation aims to compensate for the possible evaporation losses of barium at elevated temperatures during the annealing process and to prevent the formation of secondary non-magnetic phases, such as $BaFe_2O_4$ or unreacted Fe_2O_3. The required amounts of metal ions were dissolved in deionized water and stirred at room temperature for 25 minutes. Citric acid was then added, and the solution was continuously stirred at 80 °C for an additional 30 minutes until complete dissolution was achieved. To regulate the pH to 7, ammonia was gradually introduced into the solution. The mixture was then heated at 150 °C for 2 hours, followed by an increase in temperature to 300 °C to remove water and obtain a viscous gel-like solution. The combustion of the formed mass resulted in gas evolution and sustained burning, yielding a powder precursor. Finally, to refine the nanostructure and eliminate residual impurities, the obtained powder was annealed at 1100 °C for 6 hours. A schematic representation of the synthesis steps is shown in Figure 1.

Fig. 1. Schematic representation of the sol-gel synthesis of $BaFe_{12}O_{19}$ via the self-combustion reaction: (a) solution-to-gel transition, (b) auto-combustion at 300 °C, and (c) final powder obtained after annealing.

2.2. Synthesis of $BaFe_{12}O_{19}$/rGO nanocomposites

For the fabrication of nanocomposites with different reduced graphene oxide (rGO) contents, the synthesized $BaFe_{12}O_{19}$ (BFO) powder and rGO powder were separately dispersed in ethanol to ensure proper distribution. Each suspension underwent ultrasonic treatment for 30 minutes to break up agglomerates and enhance dispersion. After this step, the rGO suspension was incrementally added to the BFO dispersion, followed by an additional 30 minutes of sonication to promote uniform mixing at the nanoscale. The resulting homogeneous mixture was then transferred to an oven and dried at 60 °C for 6 hours to remove residual solvent, yielding a fine composite powder. The nanocomposites were prepared with rGO weight fractions of 10%, 20%, 40%, and 50%, and were designated as BFO-10rGO, BFO-20rGO, BFO-40rGO, and BFO-50rGO, respectively.

2.3. Characterization

The structural characteristics of the samples were analyzed using X-ray diffraction (XRD, ASENWARE AW-XDM300, Taiwan) with Cu Kα1 radiation (λ = 0.15406 nm). Surface morphology and elemental composition of the nanocomposites were examined via Field Emission Scanning Electron Microscopy (FESEM, Sigma 300-HV, Zeiss, Germany) coupled with energy-dispersive X-ray spectroscopy (EDX, integrated with the FESEM system). Optical properties were investigated using diffuse reflectance spectroscopy (DRS, Shimadzu UV3600) over the wavelength range of 300–1100 nm. Magnetic behavior, including hysteresis loops, was measured at room temperature using a vibrating sample magnetometer (VSM, Weistron VSM1100, Taiwan) under a maximum external magnetic field of 0.8 T.

3. Results and Discussion

3.1. X-ray diffraction

Fig. 2 illustrates X-ray diffraction patterns of the synthesized $BaFe_{12}O_{19}$ and $BaFe_{12}O_{19}$/rGO nanocomposites with varying percentages. The XRD patterns confirm the presence of the BFO phase (JCPDS 01-084-0757), with diffraction from hkl planes of (110), (107), (114), (203), (205), (206), (1011), (209), (217), (2011), (220), and (2014), of the hexagonal structure, with P63/mmc space group (a =b = 5.894 Å, and c = 23.215 Å) [24]. Furthermore, in the composite samples, diffraction peaks corresponding to the (002) plane of the rGO phase are clearly observed [25]. The average nano crystallite size was determined using the Scherrer equation [26]:

$$D = \frac{K\lambda}{\beta\cos\theta} \quad (1)$$

in this equation D is crystallite size, K is a shape-dependent constant with a typical value of 0.9, $\lambda(1.54\text{Å})$ indicates the incoming X-ray wavelength, β corresponds to the full width at half maximum (FWHM) of the relevant diffraction peak expressed in radians, and θ stands for the Bragg diffraction angle. Table 1 summarizes the average crystallite sizes and lattice parameters of the studied phases. For the pure BFO sample, the crystallite size calculated using the Scherrer equation was 49 nm.

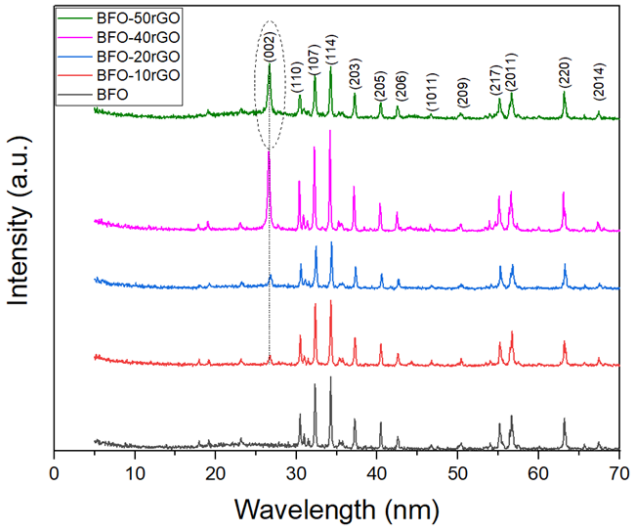

Fig. 2. XRD patterns for the BFO and BFO-xrGO nanocomposites (x = 10, 20, 40, 50 wt.%).

Fig. 3 presents the Williamson–Hall (W–H) plots constructed using the W–H equation (Eq. 2) [27]:

$$\beta Cos\Theta = 4\varepsilon Sin\Theta + \frac{K\lambda}{D} \quad (2)$$

Where ε represents the lattice strain. The diffraction peaks corresponding to (110), (107), (114), (203), (205), (2017), and (2011) were utilized for these plots. The W–H method yielded smaller crystallite size values compared to those calculated with the Scherrer equation, which can be attributed to lattice strain. Additionally, the dislocation density (δ) calculated using Eq. 3 [28], along with the strain values, are presented in Table 1.

$$\delta = \frac{1}{D^2} \quad (3)$$

Upon forming the composite with rGO, there is an overall trend of decreasing crystallite size. The strain and dislocation density within the lattice show a slight increase. The reduction in crystallite size after the addition of rGO can be attributed to the presence of the rGo matrix, which may hinder the crystal growth.

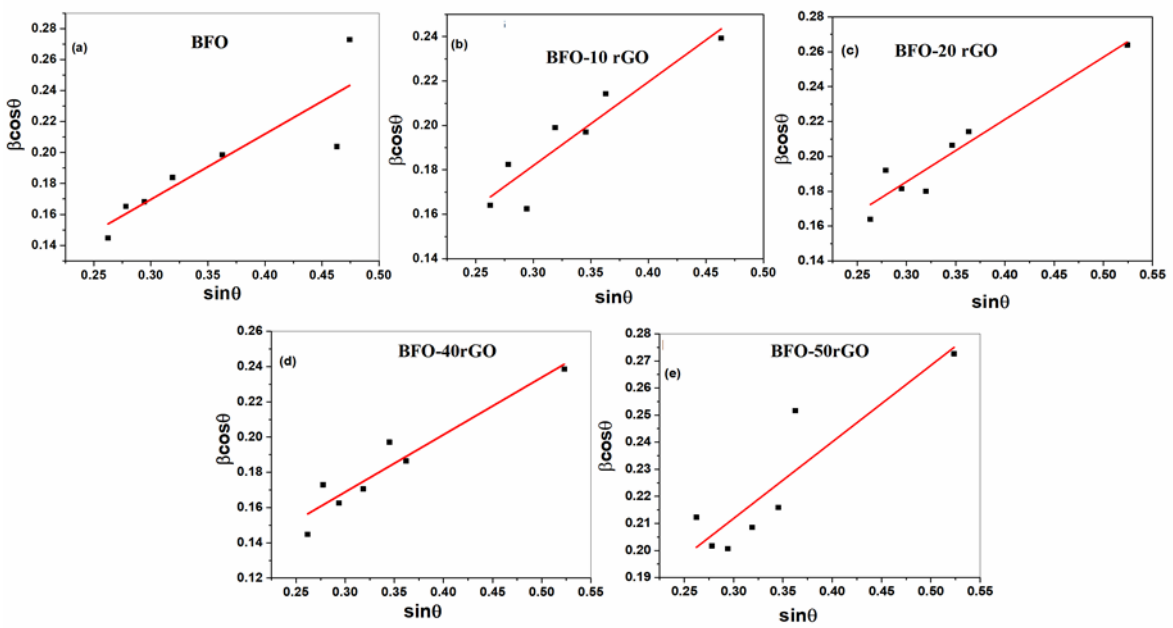

Fig. 3. W-H diagrams for the nanocomposites (a) BFO, (b) BFO-10rGO, (c) BFO-20rOG, (d) BFO-40rGO, and (e) BFO-50rGO.

Table 1. Structural Parameters Derived from XRD Analysis.

Sample	Crystallite size(nm) (Scherrer)	Crystallite size(nm) (W-H)	Strain	δ (nm^{-2})
BFO	49	34	0.010	0.0008
BFO-10rGO	46	23	0.015	0.0018
BFO-20 rGO	43	21	0.019	0.0022
BFO-40 rGO	42	20	0.017	0.0022
BFO-50 rGO	27	16	0.031	0.0039

3.2. FE-SEM analysis

The surface characteristics of the nanocomposites were examined using Field Emission Scanning Electron Microscopy (FESEM), and the resulting images are presented in Figure 4 at scale bars of 100 nm and 1 µm (inset). The pure $BaFe_{12}O_{19}$ sample exhibits a mixture of plate-like and rod-like grains with square cross-sections. Upon the incorporation of rGO, significant changes in particle size, distribution, and morphology are observed, highlighting the influence of rGO on the growth and aggregation of nanoparticles. A closer look at the particle size histogram reveals an unexpected trend the average particle size increases with higher rGO content. This phenomenon can be attributed to the agglomerative effects of rGO, which serves as a substrate for particle growth and promotes interconnection among nanoparticles. The effect is more pronounced in the BFO-40rGO and BFO-50rGO samples. Furthermore, this increase in particle size could result from changes in ion migration pathways and crystal growth control, ultimately leading to enhanced densification and structural modifications in the nanocomposites [29].

As illustrated in Figure 5, energy-dispersive X-ray spectroscopy (EDX) was employed to support the FESEM results by verifying the variations in elemental composition among the samples. This technique also provides a semi-quantitative estimation of the rGO content present in the material. As the rGO content increases, the carbon concentrations rise, while the barium and iron levels decrease. These findings validate the effective incorporation of rGO into the nanocomposite structure, altering the material's physical and chemical properties and these structural changes influence the magnetic, optical, and mechanical properties of the material.

To further verify the elemental distribution and compositional uniformity of the $BaFe_{12}O_{19}$ /rGO nanocomposites, EDS elemental mapping was carried out for the elements C, O, Fe, and Ba. The mapping results for all samples (Fig. 6) clearly demonstrate a homogeneous dispersion of $BaFe_{12}O_{19}$ particles over the rGO sheets.

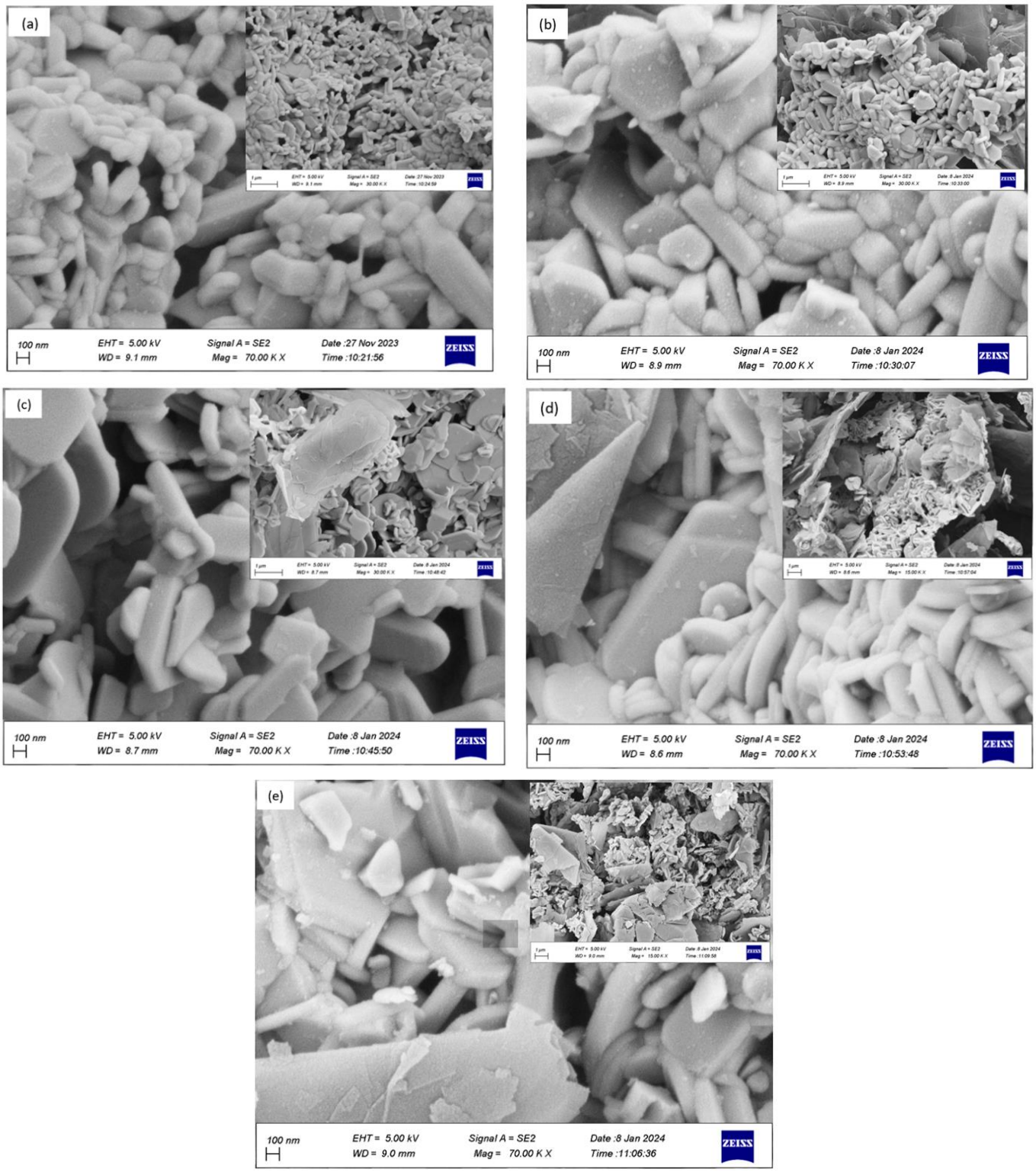

Fig. 4. FESEM images of the nanocomposites (a) BFO (b) BFO-10rGO (c) BFO-20 rGO (d) BFO-40 rGO, and (e) BFO-50rGO at scale bars of 100 nm and 1 μm (inset).

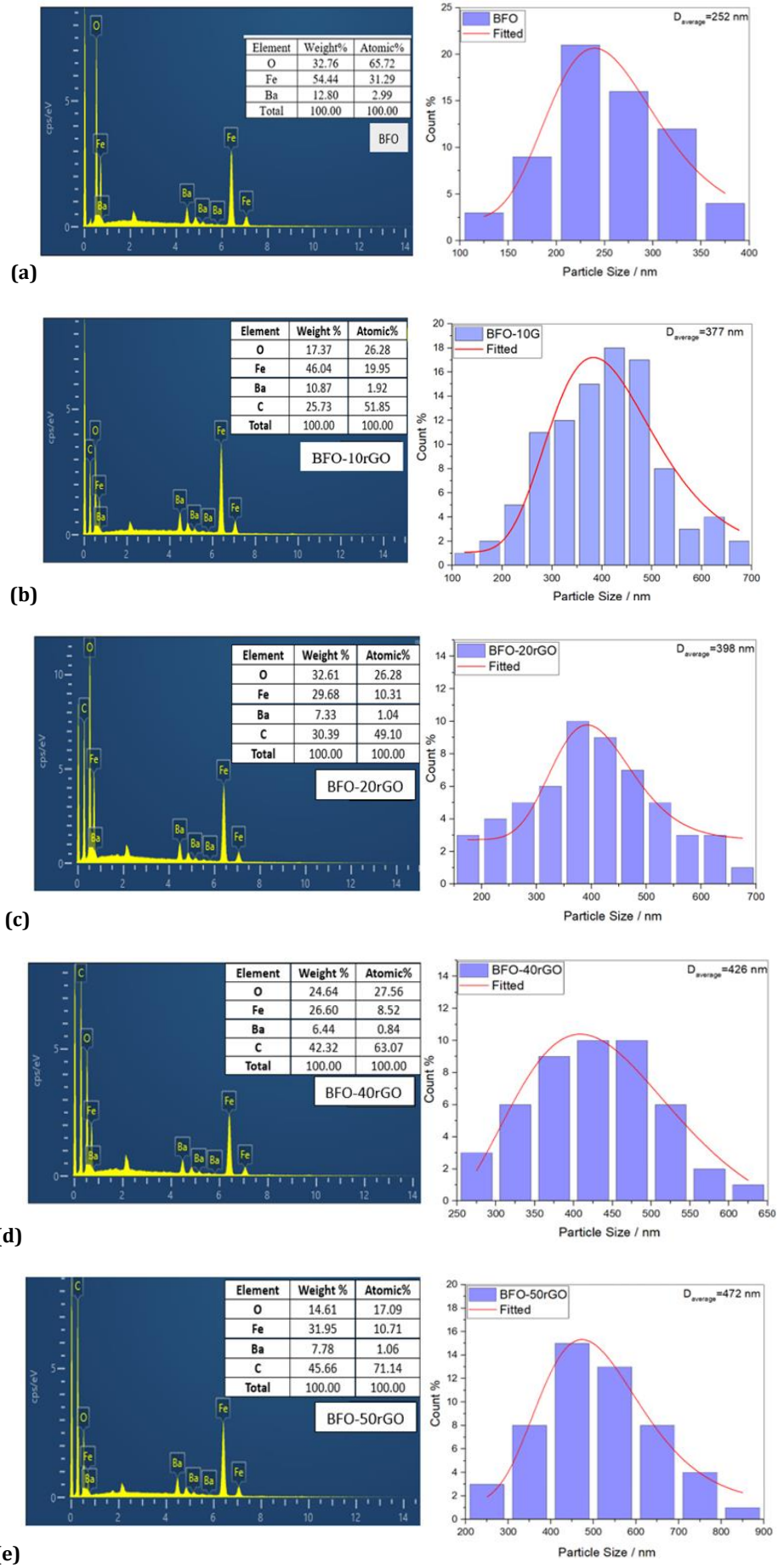

Fig. 5. EDX spectra of the nanocomposites (a) BFO, (b) BFO-10rGO, (c) BFO-20 rGO, (d) BFO-40 rGO, and (e) BFO-50rGO.

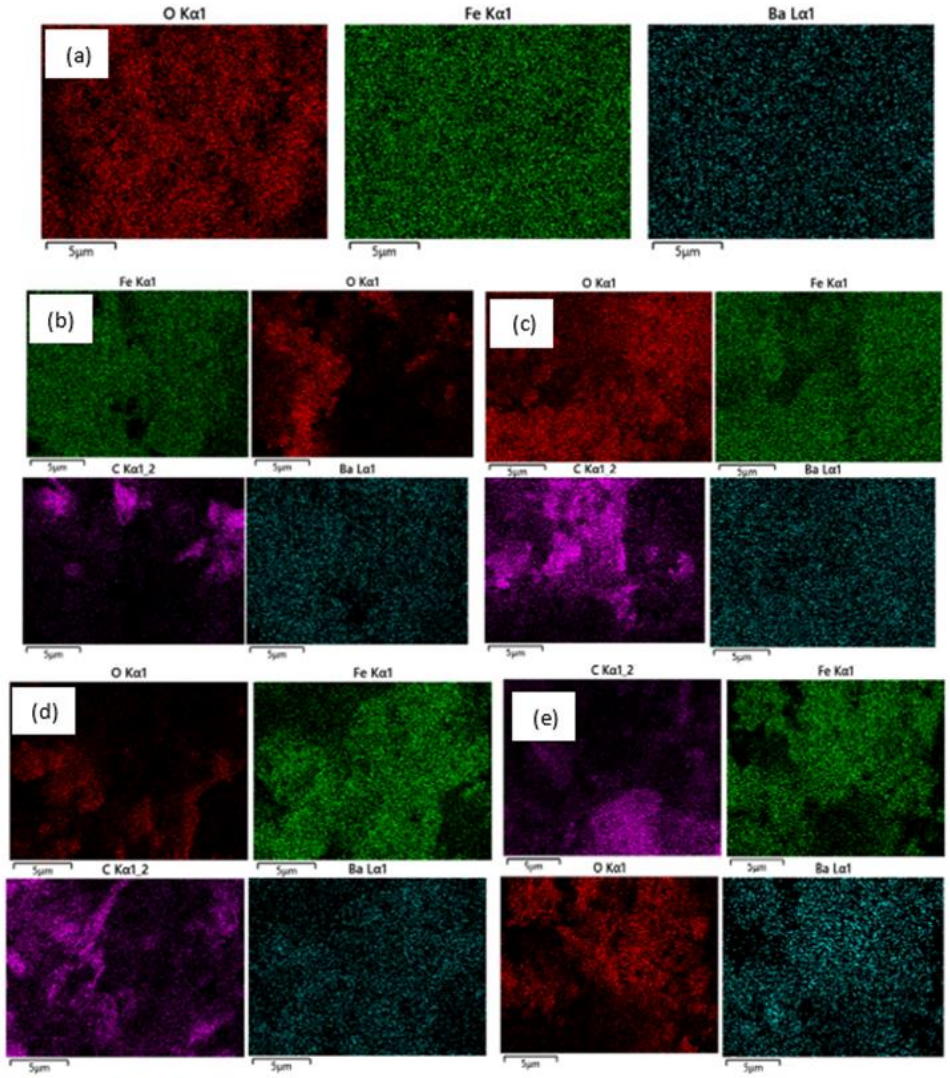

Fig. 6. EDS elemental mapping images of the samples: (a) BFO, (b) BFO–10rGO, (c) BFO–20rGO, (d) BFO–40rGO, and (e) BFO–50rGO, showing the distribution of C, O, Fe, and Ba elements.

3.3. Optical study

The optical properties of the nanocomposites were evaluated using the UV–visible method, generating diffuse reflectance spectroscopy (DRS) spectra. Figure 7 shows the absorption spectra of the prepared samples over the 300–1100 nm wavelength range. The samples exhibit maximum absorbance in the visible region (300–700 nm), followed by a gradual decrease at longer wavelengths. A sharp decline is observed in the 700 nm -750 nm range, marking the absorption edge for all samples. The absorption for the nanocomposites decreases progressively with an increase in the percentage of rGO in the visible region and an opposite behavior above the bang gap region.

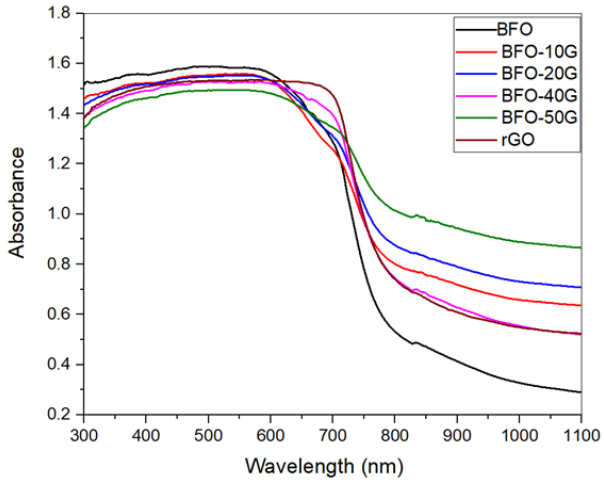

Fig. 7. Absorption versus wavelength spectra for the BFO, BFO-10rGO, BFO-20 rGO, BFO-40 rGO, BFO-50rGO, and rGO nanocomposites.

The band gap energies of all BFO/rGO nanocomposites were calculated using the well-established Tauc equation (Eq. 4), commonly employed in optical analysis [30]:

$$Ah\nu=B(h\nu - E_g)^n \quad (4)$$

where A is the optical absorbance obtained from the DRS spectrum. The absorbance data A were used as a proxy for the optical absorption coefficient (α), while B is a constant specific to the material and associated with electronic transitions. The term hν refers to the photon energy, and E_g represents the optical band gap of the substance. The exponent n defines the type of optical transition, with a value of 1/2 for allowed direct transitions and 2 for allowed indirect transitions [31,32]. The band gaps of BFO, rGO, and all nanocomposite samples were estimated based on the data illustrated in Figure 8 and summarized in Table 2. An increase in rGO content within the nanocomposite structure leads to reduction in band gap energy from 1.62 eV for pristine BFO to 1.49 eV for the BFO-50rGO sample [22,25]. This observed decrease is likely attributed to the coverage of BFO surfaces by rGO sheets, as evidenced by the morphological and structural information obtained from FESEM and XRD analyses.

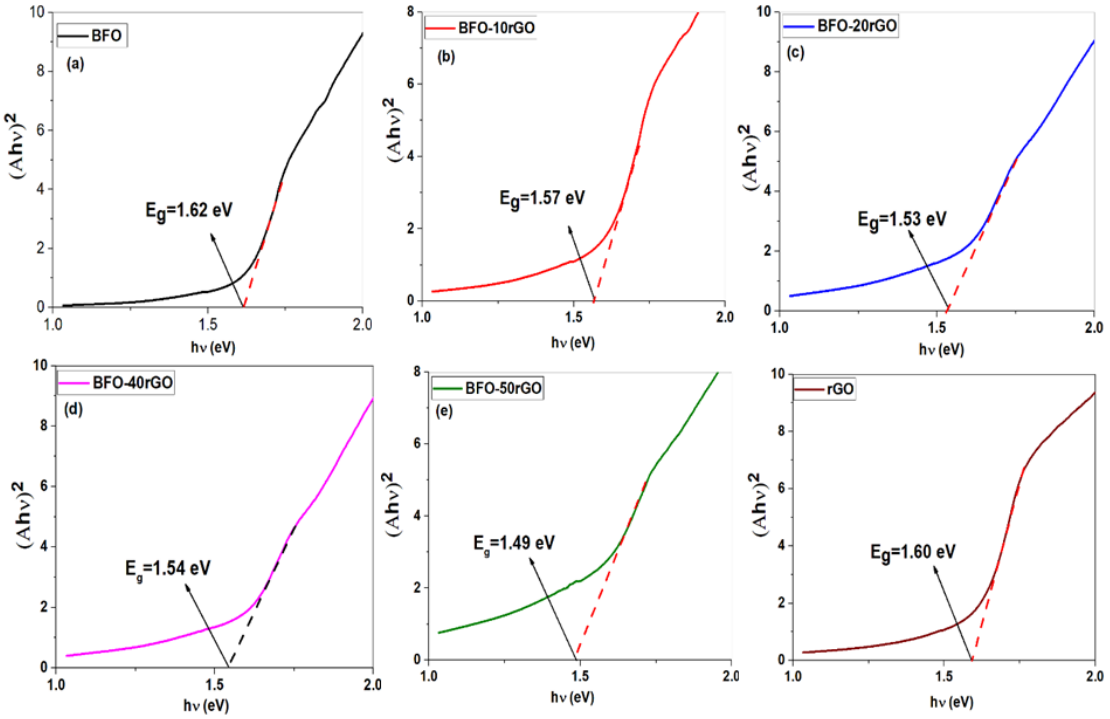

Fig. 8. Band gap diagram (Eg) for the nanocomposites (a) BFO, (b) BFO-10rGO, (c) BFO-20 rGO, (d) BFO-40 rGO, and (e) BFO-50rGO

Table 2. The band gap values determined from the optical properties.

Sample	E_g(eV)
BFO	1.62
rGO	1.60
BFO-10rGO	1.57
BFO-20rGO	1.53
BFO-40rGO	1.54
BFO-50rGO	1.48

3.4. Magnetic measurements

In order to examine the magnetic characteristics of the synthesized samples, the magnetic hysteresis loops were measured within a field range of up to 8000 Gauss at room temperature. As depicted in Figure 9, none of the samples achieved magnetic saturation within this field range. Therefore, in Figure 10, the saturation magnetization behavior of the samples was evaluated based on the law of approach to saturation, using Eq. 5 at high magnetic fields region [33]:

$$M = M_S\left(1 - \frac{a}{H} - \frac{b}{H^2}\right) + \chi H \quad (5)$$

In this Eq. the a/H term is associated with structural imperfections, while b/H^2 reflects the influence of crystalline magnetic anisotropy, and χH represents the paramagnetic contribution of the system. The key magnetic parameters, including saturation magnetization (M_s),

coercivity (H_c), remanent magnetization (M_r), and squareness ratio (M_r/M_s), are summarized in Table 3. Among the samples, pure BFO exhibits the highest M_s value, which gradually decreases as the rGO content increases. This decline is attributed to the incorporation of rGO a non-magnetic component into the BFO matrix [34]. Additionally, the coercivity (H_c) of the nanocomposites surpasses that of pure BFO at higher rGO concentrations. It could be because the surface anisotropy of BFO nanoparticles changed with the addition of rGO, Table 3 [35]. The slight curvature observed at high magnetic fields (referred to as a honeycomb-like appearance) can be attributed to the combined effect of the incomplete saturation of $BaFe_{12}O_{19}$ at 0.8 T and the linear paramagnetic contribution of rGO, which is accounted for in the χH term in Eq. (5).

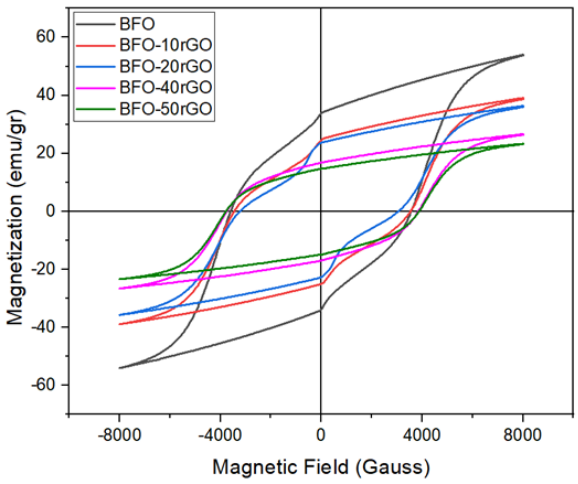

Fig. 9. Magnetic Response of BFO and BFO-xrGO Nanocomposites (x = 10, 20, 40, 50 wt%).

The incorporation of rGO powder into the $BaFe_{12}O_{19}$/rGO composite plays a crucial role in altering its magnetic characteristics. The decrease in M_r can be attributed to the magnetic dilution effect, since the incorporation of non-magnetic rGO into the BFO matrix reduces the overall magnetic moment per unit mass. Additionally, rGO contributes to variations in the coercivity of the composite and affects both the demagnetization behavior and particle size distribution. The presence of rGO introduces a certain degree of structural disorder, which may disrupt the uniform arrangement of magnetic domains, thereby reducing the overall magnetization. Moreover, the observed decrease in remanent magnetization can also be attributed to the synthesis method and the interfacial interactions between rGO and the magnetic phase. The squareness ratio (M_r/M_s), extracted from the hysteresis curves and presented in Table 3, provides useful insight into the magnetic behavior of the samples. Typically, values below 0.5 are associated with multi-domain behavior, while higher values indicate stronger remanence relative to saturation magnetization. Although all samples exhibit the squareness ratio (SQR) values greater than 0.5, this parameter alone is not sufficient to conclusively determine a single-domain state, especially under the limited applied magnetic field used in this study. Nevertheless, the observed SQR values indicate favorable magnetic characteristics that support the potential applicability of these nanocomposites in magnetic storage and memory devices [36-38].

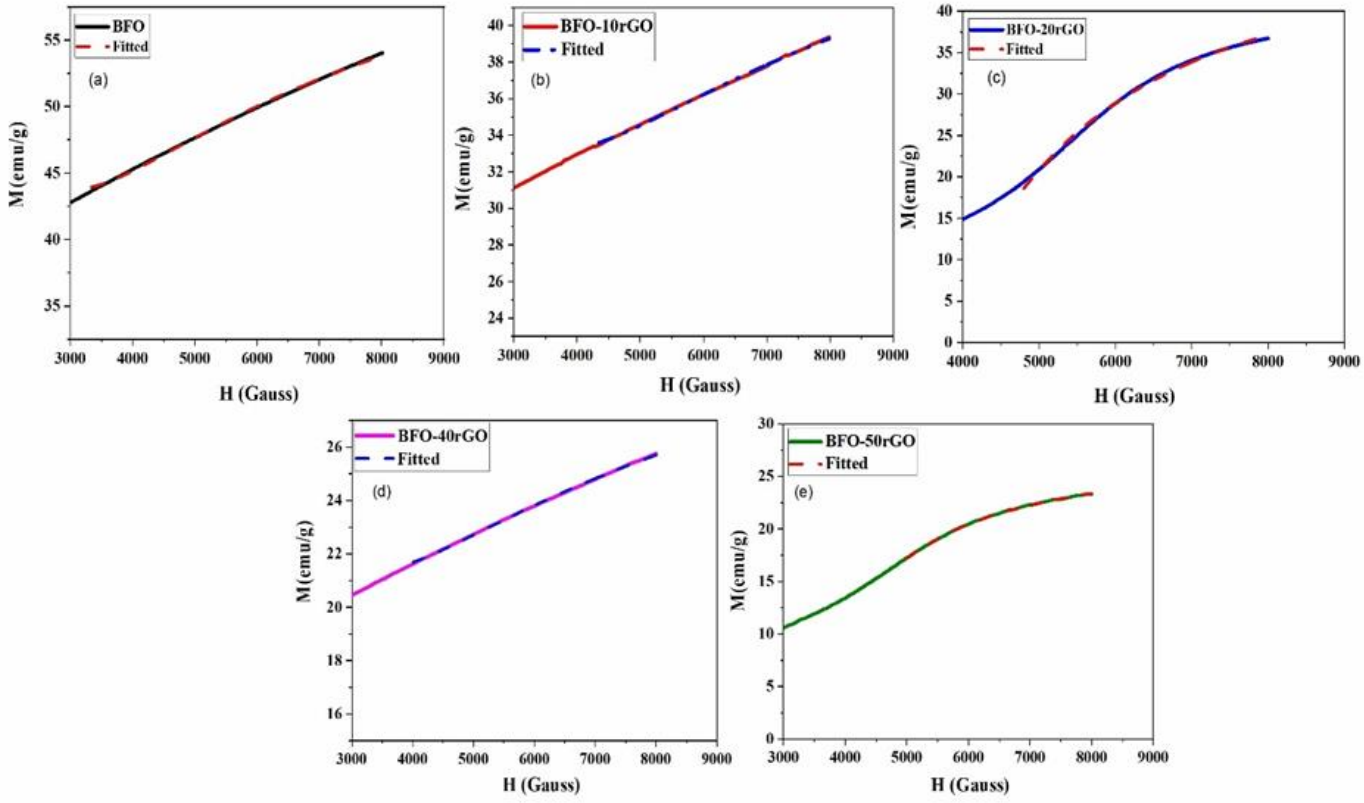

Fig. 10. Magnetization versus magnetic field at high-field regions with fitted curves for (a) BFO, (b) BFO–10 rGO, (c) BFO–20 rGO, (d) BFO–40 rGO, and (e) BFO–50 rGO nanocomposites.

Table 3. VSM-Based Extracted Parameter Summary.

Samples	H_c (Gauss)	M_s (emu/gr^{-1})	M_r (emu/gr^{-1})	SQR
BFO	3574.52	54.21	33.72	0.62
BFO-10rGO	3497.05	39.34	24.89	0.63
BFO-20rGO	3142.44	36.10	23.11	0.64
BFO-40rGO	3799.30	26.79	16.90	0.63
BFO-50rGO	3853.85	23.38	14.79	0.63

4. Conclusions

In this study, barium hexaferrite ($BaFe_{12}O_{19}$) and its nanocomposites containing 10%, 20%, 40%, and 50% rGO were successfully synthesized using the auto-combustion sol–gel method. The results indicate that the incorporation of rGO significantly influences the structural, optical, and magnetic properties of the nanocomposites. X-ray diffraction patterns confirmed the formation of the hexagonal structure of $BaFe_{12}O_{19}$, with a diffraction peak corresponding to the presence of rGO. The average crystallite size was found to decrease from 49 nm for pure $BaFe_{12}O_{19}$ to 27 nm for the composite with 50% rGOThe FESEM images revealed that the pure $BaFe_{12}O_{19}$ sample exhibited a mixture of plate-like and rod-shaped grains. As the rGO content increased, the surface morphology changed, with rGO covering the barium hexaferrite particles. The optical studies revealed that the band gap energy decreased from 1.62 eV for pure $BaFe_{12}O_{19}$ to 1.48 eV for the composite containing 50% rGO. Magnetic hysteresis measurements indicated that the saturation magnetization (M_s) of the nanocomposites decreased with increasing rGO content, from 54.21 emu/g for pure $BaFe_{12}O_{19}$ to 23.38 emu/g for the 50% rGO composite. This decline is attributed to the introduction of a non-magnetic material (rGO) into the magnetic matrix, which alters the magnetic interactions and domain alignment within the composite. Interestingly, the coercivity (H_c) values increased for the nanocomposites, suggesting that the addition of rGO enhances the magnetic stability of the material. Overall, the $BaFe_{12}O_{19}$/rGO nanocomposites exhibit promising potential for various applications, including electromagnetic interference shielding, energy storage, and advanced sensor technologies. The findings highlight the critical role of rGO concentration in tailoring the functionality of barium hexaferrite-based materials, paving the way for the development of multifunctional materials that meet the diverse requirements of modern industrial applications.

Acknowledgements

This work was supported by the Shahrood University of Technology.

Funding Statement

This research received no specific grant from any funding agency.

Conflicts of interest

The authors declare that they have no known competing financial interests or personal relationships that could have appeared to influence the work reported in this paper.

Authors contribution statement

Mona mehrabani: Acquisition of data, drafting the manuscript, analysis and/or interpretation of data, approval of the version of the manuscript to be published.

M.E. Ghazi: Conception and design of study, supervision, analysis and/or interpretation of data, revising the manuscript, approval of the version of the manuscript to be published.

References

[1] Mathews, S.A. and Babu, D.R., 2021. Analysis of the role of M-type hexaferrite-based materials in electromagnetic interference shielding. *Current Applied Physics*, 29, pp.39-53.

[2] Nikmanesh, H., Hoghoghifard, S. and Hadi-Sichani, B., 2019. Study of the structural, magnetic, and microwave absorption properties of the simultaneous substitution of several cations

in the barium hexaferrite structure. *Journal of Alloys and Compounds*, 775, pp.1101-1108.

[3] Pullar, R.C., 2012. Hexagonal ferrites: A review of the synthesis, properties and applications of hexaferrite ceramics. *Progress in Materials Science*, 57(7), pp.1191-1334.

[4] Bsoul, I., Mahmood, S.H. and Lehlooh, A.F., 2010. Structural and magnetic properties of $BaFe_{12-2x}TixRuxO_{19}$. *Journal of Alloys and Compounds*, 498(2), pp.157-161.

[5] Jasrotia, R., Singh, V.P., Kumar, R., Singha, K., Chandel, M. and Singh, M., 2019. Analysis of Cd^{2+} and In^{3+} ions doping on microstructure, optical, magnetic and mo¨ ssbauer spectral properties of sol-gel synthesized Ba M hexagonal ferritebased nanomaterials. *Results in Physics*, 12, pp.1933-1941

[6] Sharma, A., Jasrotia, R., Kumari, N., Kumar, S., Verma, A., Godara, S.K., Ahmed, J., Alshehri, S.M., Tamboli, A.M., Kalia, S. and Batoo, K.M., 2022. Tailoring the structural and magnetic traits of copper modified $BaFe_{12}O_{19}$ nanostructured hexaferrites for recording media application. *Journal of Magnetism and Magnetic Materials*, *564*, p.170124.

[7] Wagner, D.V., Kareva, K. V., Zhuravlev, V. A., Dotsenko, O.A. and Minin, R.V., 2023. Investigation of $BaFe_{12}O_{19}$ hexaferrites manufactured by various synthesis methods using a developed pulsed magnetometer. *Inventions*, 8(1), p.26.

[8] Dong, W., Zhang, Y., Yang, J., Song, H., Bai, W. and Tang, X., 2018. The effect of film/electrode interfaces on the dielectric responses of highly (000l)-oriented M-type $BaFe_{12}O_{19}$ thin films synthesized using chemical solution deposition. *Applied Physics Letters*, 113(26).

[9] Goel, S., Garg, A., Gupta, R.K., Dubey, A., Prasad, N.E. and Tyagi, S., 2020. Development of RGO/ $BaFe_{12}O_{19}$ -based composite medium for improved microwave absorption applications. *Applied Physics A*, 126, pp.1-11.

[10] Khan, I.S. and Gul, I.H., 2022. Comparative investigation of magnetic, di-electric, optical, and electrical properties of mono-$BaFe_2O_4$ and hexa- $BaFe_{12}O_{19}$ nano-ferrites for photovoltaic (PV) applications. *Applied Physics A*, 128(12), p.1109.

[11] Sazelee, N.A., Idris, N.H., Din, M.M., Mustafa, N.S., Ali, N.A., Yahya, M.S., Yap, F.H., Sulaiman, N.N. and Ismail, M., 2018. Synthesis of BaFe12O19 by solid state method and its effect on hydrogen storage properties of MgH2. *International Journal of Hydrogen Energy*, *43*(45), pp.20853-20860.

[12] Alonso-Rodríguez, D.W., Ruiz-Luna, H., Alfaro-Cruz, M.R., Bañuelos-Frias, A., Alvarado-Perea, L. and Valero-Luna, C., 2020. Synthesis and characterization of $BaFe_{12}O_{19}$ -WC catalysts prepared by mechanical milling. *Fuel*, 280, p.118608.

[13] Jebanisha, B., Devi, V.M., Varghese, J. and Aswathy, N.R., 2024. Magnetic and dielectric characteristics of rGO modified BFO nanoparticles produced using sol-gel via auto-combustion method. *Ceramics International*, 50(19), pp.36955-36963.

[14] Piracha, M.I., Murtaza, G., Imranullah, M. and Hussain, S., 2022. Reduced graphene oxide containing barium hexaferrite composites for high frequency microwave absorption. *Bulletin of Materials Science*, 45(1), p.41.

[15] Soldano, C., Mahmood, A. and Dujardin, E., 2010. Production, properties and potential of graphene. *Carbon*, 48(8), pp.2127-2150.

[16] Mbayachi, V.B., Ndayiragije, E., Sammani, T., Taj, S. and Mbuta, E.R., 2021. Graphene synthesis, characterization and its applications: A review. *Results in Chemistry*, *3*, p.100163.

[17] Tang, X.T., Wei, G.T., Zhu, T.X., Sheng, L.M., An, K., Yu, L.M., Liu, Y. and Zhao, X.L., 2016. Microwave absorption performance enhanced by high-crystalline graphene and $BaFe_{12}O_{19}$ nanocomposites. *Journal of Applied Physics*, *119*(20).

[18] Ali, K.A., Ravikumar, M.M., Mohammed, J., Farouk, N., Mohanavel, V. and Ravichandran, M., 2021. Investigation of Ku band microwave absorption of three-layer $BaFe_{12}O_{19}$, carbon-fiber@ Fe_3O_4, and graphene@ $BaFe_{12}O_{19}$ @ Fe_3O_4 composite. *Journal of Alloys and Compounds*, 884, p.161045.

[19] Yang, H., Ye, T., Lin, Y. and Liu, M., 2015. Preparation and microwave absorption property of graphene/ $BaFe_{12}O_{19}$ /CoFe2O4 nanocomposite. *Applied Surface Science*, 357, pp.1289-1293.

[20] Jie, L., Zhaohuan, Z., Zijing, D., Min, C., Runjun, S., Jiang, D., Caiting, H., Binghui, Z. and Yunyu, L., 2024. $BaFe_{12}O_{19}$/graphene/polyaniline coatings for flexible fabrics with enhanced microwave absorption. *Textile Research Journal*, *94*(3-4), pp.494-507.

[21] Wang, H., Liu, Y. and Zhao, X., 2024. Flexible and firm multilayer $BaFe_{12}O_{19}$ /GO coated composite fabric for high-performance electromagnetic shielding and wave absorption. *Progress in Organic Coatings*, 195, p.108676.

[22] Mehrabani, M., Ghazi, M. E., & Izadifard, M., 2024. Influence of GO content on the optical, magnetic and dielectric properties of the $BaFe_{12}O_{19}$ /GO nanocomposites. *Physica Scripta*, 99(9), p.095923.

[23] Almessiere, M.A., Slimani, Y., Tashkandi, N.A., Baykal, A., Saraç, M.F., Trukhanov, A.V., Ercan, İ., Belenli, İ. and Ozçelik, B., 2019. The effect of Nb substitution on magnetic properties of $BaFe_{12}O_{19}$ nanohexaferrites. *Ceramics International*, *45*(2), pp.1691-1697.

[24] Anjum, S., Hameed, S., Awan, M.S., Amed, E. and Sattar, A., 2017. Effect of strontium doped M-Type bariam hexa-ferrites on structural, magnetic and optical properties. *Optik*, *131*, pp.977-985.

[25] Soomro, S.A., Gul, I.H., Naseer, H., Marwat, S. and Mujahid, M., 2019. Improved performance of $CuFe_2O_4$/rGO nanohybrid as an anode material for lithium-ion batteries prepared via facile one-step method. *Current Nanoscience*, *15*(4), pp.420-429.

[26] Bokuniaeva, A.O. and Vorokh, A.S., 2019, December. Estimation of particle size using the Debye equation and the Scherrer formula for polyphasic TiO_2 powder. *In journal of physics: Conference series* (Vol. 1410, No. 1, p. 012057). IOP Publishing.

[27] Nath, D., Singh, F. and Das, R., 2020. X-ray diffraction analysis by Williamson-Hall, Halder-Wagner and size-strain plot methods of CdSe nanoparticles-a comparative study. *Materials Chemistry and Physics*, 239, p.122021.

[28] Mustapha, S., Ndamitso, M.M., Abdulkareem, A.S., Tijani, J.O., Shuaib, D.T., Mohammed, A.K. and Sumaila, A. (2019). Comparative study of crystallite size using Williamson-Hall and Debye-Scherrer plots for ZnO nanoparticles. *Advances in Natural Sciences: Nanoscience and Nanotechnology*, 10(4), p.045013.

[29] Mandizadeh, S., Soofivand, F., Salavati-Niasari, M. and Bagheri, S., 2015. Auto-combustion preparation and characterization of $BaFe_{12}O_{19}$ nanostructures by using maleic acid as fuel. *Journal of Industrial and Engineering Chemistry*, 26, pp.167-172.

[30] Jin, Y., Zheng, Y., Podkolzin, S. G. and Lee, W., 2020. Band gap of reduced graphene oxide tuned by controlling functional groups. *Journal of Materials Chemistry C*, *8*(14), pp.4885-4894.

[31] Jubu, P.R., Adedokun, O., Mbakaan, C., Nathan-Abutu, A., Danladi, E., Tsaviv, J.N., Kyesmen, P.I., Akeredolu, B.J., Adepoju,

A.T., Aungwa, F. and Yusof, Y., 2025. Accuracy in estimating the absorption coefficient of powdered nanomaterials: resolving misconceptions in tauc plot application for energy bandgap determination. *Journal of Materials Science: Materials in Electronics*, *36*(16), p.961.

[32] Pankove, J.I., 1975. Optical processes in semiconductors. Courier Corporation.

[33] Durmus, Z., 2015. A comparative study on magnetostructural properties of barium hexaferrite powders prepared by polyethylene glycol. *Journal of Nanomaterials*, 2014, pp.212-212.

[34] Moatoshi, Borgohain, C., Kaushik, S.D. and Borah, J.P., 2023. Impact of transition metal (Co and Mn) substitution on the structural and magnetic properties of $BaFe_{12}O_{19}$ nanoparticles towards permanent magnet application. *Applied Physics A*, *129*(9), p.607.

[35] El-Khawas, E.H., Azab, A.A. and Mansour, A.M., 2020. Structural, magnetic and dielectric properties of reduced graphene oxide/$La_{0.9}Bi_{0.1}FeO_3$ nanocomposites. *Materials Chemistry and Physics*, 241, p.122335.

[36] Cullity, B.D. and Graham, C.D., 2011. *Introduction to magnetic materials*. John Wiley & Sons.

[37] Singh, V.P., Jasrotia, R., Kumar, R., Raizada, P., Thakur, S., Batoo, K.M. and Singh, M., 2018. A current review on the synthesis and magnetic properties of M-type hexaferrites material. *World Journal of Condensed Matter Physics*, *8*(02), p.36.

[38] Bitaraf, M., Ghazi, M.E. and Izadifard, M., 2023. $CoFe_2O_4$-$BaTiO_3$ nanocomposites; role of ferrite phase on the structural, optical and magnetic properties. *Ferroelectrics*, 613(1), pp.231-249.